Available online at www.sciencedirect.com
SCIENCE DIRECT®
Journal of Computational Physics 217 (2006) 200–216
JOURNAL OF COMPUTATIONAL PHYSICS
www.elsevier.com/locate/jcp

Uncertainty quantification for chaotic computational fluid dynamics ☆

Y. Yu [b,*,1], M. Zhao [b,1], T. Lee [b,1], N. Pestieau [b,1], W. Bo [b,1], J. Glimm [b,c,1,2,3], J.W. Grove [a,4]

[a] *Los Alamos National Laboratory, Los Alamos, NM 87545, United States*
[b] *Department of Applied Mathematics and Statistics, State University of New York at Stony Brook, Stony Brook, NY 11794-3600, United States*
[c] *Computational Science Center, Brookhaven National Laboratory, Upton, NY 11973, United States*

Received 15 August 2005; received in revised form 16 March 2006; accepted 27 March 2006
Available online 26 May 2006

Abstract

We seek error models for simulations that model chaotic flow. Stable statistics for the solution and for the error are obtained after suitable averaging procedures.

Keywords: Uncertainty quantification; Chaotic flow

1. Introduction

Uncertainty quantification is at its essence a study of errors, both their description and their consequences. Addressed here are the errors arising from the finite resolution numerical discretizations used to obtain solutions. In this sense, the problem, a bit simplistically, can be viewed as the determination of error bars to be assigned to the numerical solution algorithms. For a Bayesian decision framework which leads to this point of view see [9,10]. Our approach to numerical solution errors is motivated by needs of uncertainty

☆ LANL preprint number LA-UR-05-6212.

* Corresponding author. Tel.: +1 631 632 9360; fax: +1 631 632 8490.
E-mail address: yan2000@ams.sunysb.edu (Y. Yu).

[1] Supported in part by the U.S. Department of Energy Grant DE-FG02-90ER25084 and the Los Alamos National Laboratory, Contract 14816-001-05.
[2] Supported in part by the NSF Grant DMS-0102480.
[3] This manuscript has been co-authored by Brookhaven Science Associates, LLC, under Contract No. DE-AC02-98CH1-886 with the U.S. Department of Energy. The United States Government retains, and the publisher, by accepting this article for publication, acknowledges, a world-wide license to publish or reproduce the published form of this manuscript, or allow others to do so, for the United States Government purposes.
[4] Supported in part by U.S. Department of Energy.

0021-9991/$ - see front matter
doi:10.1016/j.jcp.2006.03.030

quantification. A key ingredient of the Bayesian approach is the likelihood of a mismatch between the predicted (simulated) event and the true event. The mismatch has several components: solution error, theoretical or modeling error or approximation, experimental error, etc. Specifically the Bayesian likelihood is (up to normalization) a probability, which specifies probability of occurrence of an error of any given size. Unlike other authors [11,3,12,5] who usually use observational errors or expert opinion to form a probability model for the likelihood, our approach is to use solution error models for the likelihood. In this sense, we address the solution error contribution only to the total mismatch likelihood. We believe the physics modeling error, generally considered to be more intractable, should be treated in the same spirit, by observing the solution variation as the physics model is refined.

It is common to think of uncertainty as originating in the underspecification of the problem, such as the initial conditions or some physics parameter. The unknown inputs have probability distributions, and the solution operator (regarded as deterministic, in contrast to our approach) maps input probabilities into output probabilities. To transform these higher dimensional objects (probabilities of inputs) into outputs, also higher dimensional, an efficient representation of the transformation is needed. For this purpose the Wiener path or Polynomial Chaos expansion is used to approximate the input descriptions and map them to output descriptions [23,14,6,19]. This approach is complimentary to that taken here. We have a stochastic solution mapping, rather than or in addition to a stochastic input. Even if we have a stochastic input, we use a very simple description of it, based on means and variances, without the use of higher moments, as would occur in the case of a Wiener expansion.

Since many simulations are under resolved, as used in practice, asymptotic analysis of convergence does not address the issue of error bars and uncertainty quantification, and for hyperbolically dominated flows, with poor theoretical foundations, a posteriori methods are generally inapplicable. The method of a posteriori analysis aims to construct an upper bound on the solution error, either theoretically validated or based on numerical experiments [1,18,21,4]. This method has been difficult to apply to non-linear hyperbolic systems, and in any case does not answer the questions addressed here. We seek to characterize the error, not just to bound it. For this reason, we consider errors from a statistical point of view, and examine an ensemble of coarse and fine grid pairs, and their differences, which are assumed to represent the coarse grid solution error.

The statistical approach to error analysis is simple and robust, but its direct application fails for the problems considered here, namely chaotic CFD. By definition, chaotic flows are ones which exhibit sensitive dependence on initial conditions. Generally, they also exhibit sensitive dependence on other parameters, not only the physical parameters which define the flow, but also the numerical parameters which define the solution algorithm.

There is no shortage of important chaotic flow problems. We mention climatology [15], turbulence [2,16], fluid mixing [20], flow in porous media [13], and turbulent combustion [17]. Here we consider a representative but relatively simple chaotic flow, the Richtmyer–Meshkov instability resulting from a shock passing through a density discontinuity. We consider this problem in a perturbed circular (2D) geometry. Namely, a circular shock wave implodes a perturbed circular interface, and the two circles may or may not be offset relative to one another. The shock proceeds to the origin, where it is reflected, and the reflected shock reshocks the now highly perturbed interface, giving rise to a highly chaotic flow. See Fig. 1.

The L_1 convergence for this problem is displayed in Fig. 2, left frame. Here we measure errors as the difference between the current and the finest grid solutions, and the convergence is perhaps 1/2 order in the grid spacing, Δx, but decreasing as time progresses. If the error were measured (as we do in the rest of the paper) by comparing consecutive grid sizes (separated by a factor of 2), the corresponding plot would show non-convergence for late time. While these two measures of convergence order will show identical exponents in an asymptotic regime, the current problem is not, and perhaps due to the chaotic nature of the solution, cannot be in the asymptotic regime. The global L_1 norm masks convergence difficulties that we will explore in detail.

L_∞ norms of the error (not displayed) do not converge. It is well known that position errors in shock discontinuities give rise to constant (non-convergent) L_∞ error norms. The same statement applies to contact or interface discontinuities. The new feature we address in this paper is that the interface, for this chaotic problem, is nearly a volume, rather than a surface effect (as it is in some sense fractal), and is non-convergent. See Fig. 2, right frame, which displays the divergence of the time dependent interface length under mesh refinement.

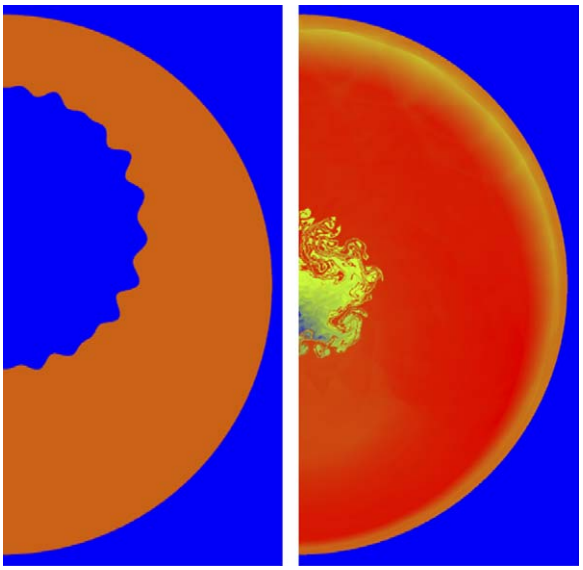

Fig. 1. Left: Initial geometry of a circular shock imploding a perturbed circular contact discontinuity. The two circles are offset relative to each other. Right: Chaotic flow observed after reshock by the outgoing shock reflected from the origin. Gray scale in both plots indicates density. The grid is 1600×3200.

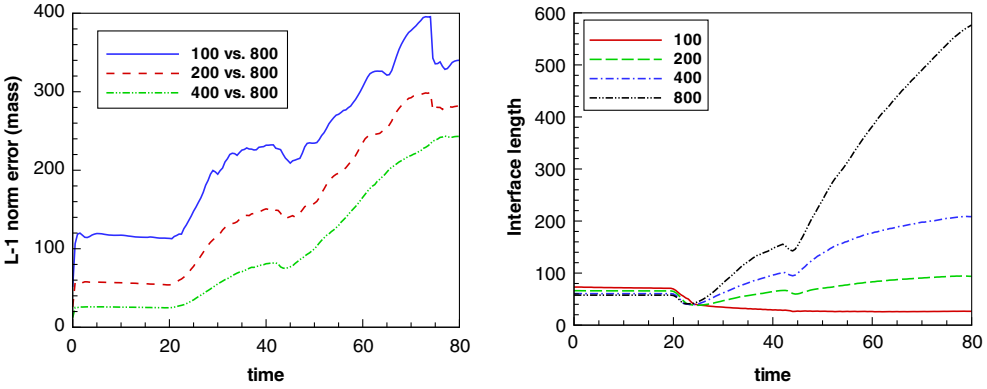

Fig. 2. Left: L_1 norms of the errors for successive grid levels (convergent). Right: Interface length for successive grid levels (divergent). Non-offset case.

We eliminate much of the source of this chaotic behavior by examination of single phase quantities, such as the light or heavy fluid density.

In assessing convergence and convergence orders, we combine the effects of the mean error (M) and the standard deviation (STD) of the error. Following conventional ideas, we assess convergence order in terms of the quantity $|M| + 2$ STD. For the light and heavy phase densities, averaged over an angular arc, this quantity is convergent. But the order and the rate of convergence depends on the fluid type (heavy vs. light, single phase vs. mixed phase) and region, and may depend on the realization. Volume fractions and other statistical measures of the mixing and of the interface require greater care in the study of their convergence. We summarize in an approximate manner in Table 1 the data on convergence order presented in later sections.

The light fluid is located near the origin, where there are repeated shock, rarefaction and compression wave reflections. Only the leading one of these has been removed from the light fluid convergence statistics, while all of them give rise (at the present levels of grid refinement) to local singularities in the solutions and the errors. It is apparently for this reason that the doubly shocked light fluid convergence is lower order. Even for quantities with identical convergence orders, we observe distinct behavior, in the form of distinct coefficients multiplying

Table 1
Summary of convergence properties and orders, for the heavy and light densities ρ_h and ρ_l, volume fraction β, shock position s and mixing zone edges mz

1st order or near 1st order	Marginal or $\approx 1/2$ order	Non-convergent
$\rho_h(r,t,\xi)$	$\rho_h(r,t,\xi)$ doubly shocked and mixed phase regions	$\rho_h(r,t,\xi)$ mixed phase region
$\rho_h(r,t)$ singly and doubly shocked regions	$\rho_h(r,t)$ mixed phase region	
$\rho_l(r,t,\xi)$ singly shocked and mixed phase regions	$\rho_l(r,t,\xi)$ mixed phase and doubly shocked regions	
$\rho_l(r,t)$ singly shocked	$\rho_l(r,t)$ doubly shocked and mixed phase regions	
	$\beta(r,t,\xi)$, $\beta(r,t)$	$\beta(r,t,\xi)$ doubly shocked region
$s(t,\xi)$, $s(t)$		
$mz(t,\xi)$, $mz(t)$ width		
	$mz(t,\xi)$, $mz(t)$ centerline	

All quantities are averaged over an angular variable, and also over all variables not explicitly present in the table. The variable ξ is an ensemble realization variable. The same quantities located in distinct columns indicate possible qualitatively different convergence behavior for distinct realizations, or for different angular regions, or as a distinction between offset and non-offset behavior.

a power of Δx, for distinct regions within the solution, and possible dependence on the realization within the ensemble. The angular averages are essential within the mixing zone to be able to compare similar solution features with possibly different locations, and these averages are convenient to use throughout the entire analysis.

Because chaotic flows are important and because their study has a long history, the challenges to their description have already been recognized. These challenges have also been addressed, most vigorously in the analysis of observational or experimental data. An experimentalist will call a quantity reproducible or observable if repeated measurements yield nearly identical values. For obvious reasons, experimentalists deal only with reproducible quantities. If measured quantities, which appear not to reproducible, are important, then their statistical distributions are studied, and these distributions are (hoped to be) reproducible. Thus, for example, turbulent velocity fluctuations, which are not reproducible as point values, are still reproducible in a statistical sense, and two point velocity correlations are a central object of study in turbulence modeling.

We follow the same approach for the analysis of errors in chaotic flows. We call a quantity observable or reproducible if it is convergent under mesh refinement. According to this definition and the definition of a chaotic flow, the solution point values are not observable. Thus we see that the beginning of the research program has to be the identification of observable quantities, with sufficient richness to provide a useful description of the flow.

Following the lead of our motivating examples (turbulence, climatology), we observe averaged quantities and statistically convergent probability distributions of fluctuating quantities. The averages may be spatial and/or temporal and may require integration over an ensemble of "equivalent" problems. Here we specify a probability distribution of initial interface perturbations to define the solution and the error ensemble. Obviously, too much averaging leads to degradation of the information available to describe the flow, while too little averaging leads to statistics that are noisy and difficult to interpret.

One main conclusion of our study is that only a modest amount of averaging is sufficient to define observable quantities for the problem considered here. In most cases, averaging over a circular arc of 45° suffices. For offset cases (the circular shock wave and the perturbed circular interface are offset relative to one another), averaging over a circular arc of 40° suffices. Within that circular arc, there are about two distinct perturbation modes on the random interface. The numbers 45 and 40 were obtained after numerous testing. We tested 5°, 10° and 20° arcs. Too little averaging leads to statistics that are noisy and difficult to interpret. The 45° arc averaging gives well defined variables for comparison between grid levels. Consider the density $\rho(x,y,t)$ and the heavy and light fluid densities ρ_h and ρ_l. The location of the heavy and light fluids will typically shift between grid levels, due to the chaotic nature of the mixing. Thus comparison of common fluid types, $\rho_h(x,y,t)$ for example, may not be even defined, while comparison of the globally defined ρ will compare different fluids (heavy vs. light), which is not a meaningful comparison. Some quantities, in particular the mixing zone volume fraction for the two fluids, need, beyond this angular averaging, a fair amount of ensemble averaging.

The required amount of averaging is obviously highly problem dependent. It is also "convergence" dependent in the sense that more extensive averaging will improve the convergence properties, so that with any given

convergence goal, more extensive averaging may be required. We have generally attempted a minimal level of averaging, leading to marginal convergence properties. To state our averaging in a more problem independent manner, we have averaged over about two random modes, and for some cases, up to about six elements of an ensemble for a total of $2 \times 6 = 12$ modes. With this level of averaging, we obtained at least marginal convergence for all solution quantities we considered.

Other than focusing on the uncertainty for a given grid resolution, we also seek to answer how fine a grid resolution is necessary to obtain a convergent solution. Here we presume, for the sake of definition, that a solution has converged if the error is within 5% of the fine grid solution value. The grid level to achieve this definition of convergence varies, depending on the quantity observed and the region of space-time (i.e. the solution history) for this quantity. For shock position and mixing zone edges, the errors are small, within $0.1\Delta x$ for the inward shock and $0.5\Delta x$ for the outward shock. For the coarsest grid we consider (100×200), the position is already convergent in the sense of the above definition. In Table 2, we list the grid resolution needed for a convergent solution for density (heavy fluid and light fluid) and volume fraction.

The use of the quantity $|M| + 2$ STD to measure solution error is based on an assumption that there is a unique, realization independent quantity determined by a sequence of mesh refined simulations. In this case the role of the ensemble is merely to provide alternate possible instances of the error. For some variables we find divergence in this metric (the volume fraction $\beta(r, t, \xi)$, as a function of radius, time and ensemble realization, in the doubly shocked region). For the non-convergent quantities, this assumption fails. For β, the ensemble averaged quantity converges, and we regard this as the limit.

We draw some general conclusions from the extensive details presented below.

- Convergence is not asymptotic in Δx, nor even monotone, and is not identical under minor modifications of measurement.
- The variability shows up in the standard deviation (STD), and the STD must be included when assessing reliability of a calculation.
- Errors are generally below Δx or $2\Delta x$ in position, and below 10% in density or volume fraction.
- Convergence is slow, often 1/2 order or less, and depends on the flow history.

We continue our earlier use of wave filters to automate the location of distinct solution structures. These filters locate the shock waves and the mixing zone edges; the shock waves thus located are the lead ingoing shock and its reflection from the origin, the outgoing reflected shock. Based on the wave filters, we can analyze position errors in these structures. The shock position errors give rise to solution state variable errors which are L_1 but not L_∞ convergent. The wave filters divide space and time into homogeneous regions, each possessing a more or less common history, such as the singly shocked or doubly shocked fluid, or the single or mixed phase fluid. Within a single homogeneous region, we find homogeneous error statistics. Most of the error statistics are spatially homogeneous (translation invariant) within the accuracy that we observe them. But for regions enclosing the origin, we find that the light fluid density statistics has a spatially non-uniform behavior at the origin at the time of shock arrival at the origin. This divergence can be fit to a power law $\approx cr^{-0.25}$. The power law behavior mimics the behavior of the solution itself, as was observed in our earlier 1D error studies [8]; see also [22].

Table 2
Summary of grid resolution needed for a convergent solution, for the heavy and light densities ρ_h and ρ_l, and the volume fraction β

ρ_h	Singly shocked region	100×200
	Doubly shocked region	100×200
	Mixing zone region	200×400
ρ_l	Singly shocked region	100×200
	Doubly shocked region	200×400
	Mixing zone region	400×800
β	Singly shocked region	400×800
	Doubly shocked region	800×1600

All quantities are averaged over an angular variable.

In Section 2 we introduce the wave filters and in Section 3, we formulate precisely the problem under study. In Section 4 we analyze the position errors for the shock waves and mixing zone edges that the wave filters describe. In Section 5, we analyze the solution errors within each of the regions of space time defined by the wave filters. In Section 6, we study the volume fraction and its error analysis.

2. Wave filters

A wave filter is an automated pattern recognition algorithm which locates shock wave, rarefaction wave and contact discontinuities in numerical solutions of the Euler equations for compressible fluids. In one dimension the method [7] examines states along a sequence of adjacent points, fits the jump at the end points of the sequence to a Riemann solver, and if a single wave type is detected in the Riemann solution, tries to fit the solution through all the mesh points between the two mesh points to an error function erfc or piecewise linear wave form (depending on the wave type). In [8], this algorithm was extended to two dimensional flows. Starting from an arbitrary point and in an arbitrary direction, a 1D wave filter looks for a significant indication of a single wave type. The central location and direction in which this single wave type occurs most clearly is the predictor for the wave front position and normal. The predictor for the tangent to the wave front is the normal to the predictor normal, passing through the predictor position. Finding points at unit mesh spacing along this predictor for the tangent, we repeat the 1D construction to find the best fitting position for the wave front. From this construction, we have three points on the wave front, one to the left, one to the right and one at the original location where the wave was detected. We fit a circle to these three points, giving a corrected wave front position and normal. For the present problem, with its approximate circular symmetry, and our average of state variables over a 45° angular sector, we average the shock position data in these sectors also to yield sector-averaged shock positions.

This algorithm is here applied in 2D for the first time, and we find some modifications are needed for efficiency. First, as we are only interested in the detection of shock waves, all the 1D passes only look for shock waves. Secondly, we can prune the initial search locations and directions, omitting points and directions in which an initial analysis based on solution gradients indicates no activity. The wave front data analysis is performed at a fixed time interval equal to six time steps on the coarse grid, and occupies less than 10% of the total solution time.

A new wave type, the edge (inner or outer) of the mixing zone is also needed, and for this purpose a new wave filter is constructed. We follow previously accepted ideas in the analysis of Rayleigh–Taylor mixing data, and look for the 5% and 95% volume fraction contours. For the present problem, with approximate circular symmetry, we look for the 5% and 95% volume fraction contours within a 45° sector. The location of these 5% and 95% contours can be a noisy diagnostic for the edge of the mixing zone, which occasionally moves abruptly as a function of time. While we have not solved this problem, we have avoided it for the data presented in this paper.

In Fig. 3, we plot the space time contours in r, t space for the inward and reflected shocks and for the inner and outer edges of the mixing zone. We have adjusted the tolerances in the automated filter so that it picks up exclusively the strong waves we are trying to locate (and thus misses numerous weak waves). The thresholds are set in the variable $(P_2 - P_1) \times$ (pressure ratio + Atwood number). Here P_1, P_2 are the pressures behind and ahead of the shock.

The shock wave filter does not depend on angular averaging. The angular dependence of the shock wave for a sequence of times is shown in Fig. 4. This figure illustrates the robustness of the wave filter tool in its 2D application. The ripples in the wave front in the left frame near the center (vertically) of the figure are at the time of passage of the shock front through the perturbed interface, and reflect defraction events at the shock front to advance or retard local portions of the shock front. Similar ripples occur in the outgoing shock angular dependence during its transit through the mixing zone. See Fig. 4, right frame, near the bottom.

3. Problem formulation

We consider a computational domain x, $y \in [0,25] \times [-25,25]$ (units of cm). Time units are in microseconds, and pressure is in Megabars. With r denoting the radial coordinate in the x, y plane, the initial contact

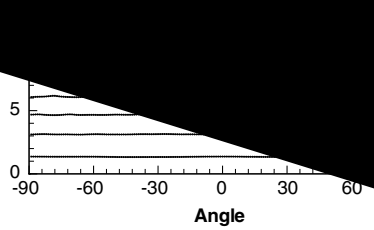

Fig. 3. Spa
(reflected)
$\theta \in [-45°,$
plots of th

interturbed from a circle at $r = 12.5$. Outside this contact is a stiffened gamma law gas, repres
parameters given approximately by $\gamma = 3.72$, $p_\infty = 0.15$, to define the stiffened gamma law pr
p, $\gamma p_\infty = (\gamma - 1)\rho e$. Inside the contact is also a stiffened gamma law gas, representing lucite, with approxi-
mate parameters $\gamma = 1.85$, $p_\infty = 0.03$. A constant pressure boundary is located at $r = 24$. The initial ambient
pressure is $p = 10^{-6}$, and the imposed pressure at the boundary is $p = 0.687$, giving rise to an inward propa-
gating Mach $M = 2$ shock at $t = 0$. The densities are approximately $\rho_{\text{tin}} = 7.3$ and $\rho_{\text{lucite}} = 1.2$ at $t = 0$, giving
an Atwood number $A = (\rho_2 - \rho_1)/(\rho_2 + \rho_1) = 0.72$. We consider a series of grids, with sizes 100×200,
200×400, 400×800, 800×1600, and 1600×3200. For brevity, each grid will be referred to through its smaller
dimension, i.e., the grid size 100 stands for a 100×200 grid. Errors will be assessed in comparison of adjacent

grid sizes, so that the error in the 100 grid is the difference between the 100 and the 200 mesh grids. The runs continue until after the passage of the reflected shock through the contact interface (reshock), and terminate before the rarefaction wave which results from the reflected shock interaction with the constant pressure boundary contaminates (very much of) the rest of the flow. For the present problem dimensions, this time is $t = 80$. With this convention, we observe errors at four levels of mesh refinement in this study. The finest level, which is needed to determine convergence in some of the variables, is carried out for a single realization, while the other grid levels are computed with an ensemble of $N = 5$. For each pair of adjacent grid levels, we assess the errors in various solution variables in terms of the mean and standard deviation, using $|M| + 2$ STD as a measure of convergence. Comparing errors at two successive grid levels, we define a convergence order as the $\ln_2$ of the ratio of the errors. If the convergence order, averaged over grid levels, is positive, we report convergence. To add to the reliability of this designation, we repeat the same analysis a number of times (multiple realizations or equivalent but different regions of space) and report recurring values, but not outliers.

The contact interface has been perturbed by sine waves to have the initial configuration

$$r(\theta) = r_0\left(1 + \sum_n a_n \sin(n\theta)\right), \tag{1}$$

$\theta \in [-\pi/2, \pi/2]$. Here $r_0 = 12.5$ and sine modes are selected so that the imposed reflection symmetry at $\theta = \pm\pi/2$ leads to a smooth curve. The sum over n ranges from $n_{\min} = 8$ to $n_{\max} = 16$, so that the average number of observed modes in the initial perturbation is about 12. The coefficients a_n are chosen as Gaussian random variables, with mean zero and STD 0.2, based on the C random number generator erand48(), mapped into a Gaussian distribution. The observed mean peak to peak amplitude, determined by this STD, is 0.25. Successive calls to the random number generator generate the ensemble of initial conditions used in this study.

For the non-offset simulations, the circles defining the pressure boundary conditions (and the initial shock) and the contact are both centered at the origin. For the offset simulations, the circle defining the (pre-perturbed) contact has a center at $x = 0$, $y = 5$.

4. Wave position errors

Our major conclusions for the analysis of wave position errors are:

1. The incoming shock wave position errors converge to zero linearly in Δx.
2. The outgoing shock position errors also converge to zero linearly in Δx, but very fine meshes are needed to observe this convergence.
3. The errors depend on the realization, i.e., even for first order errors, the coefficient of Δx in the error shows run to run variation.
4. The mixing zone edge position is meaningful only in regard to some spatial or ensemble variation. We choose here an angular arc of 45° to define the mixing zone edge.
5. The centerline of the mixing zone is less convergent than the width, and for the doubly shocked region appears to be convergent only after consideration of a highly refined mesh.

4.1. Shock wave position errors

The shock wave position errors display distinct behavior in distinct time regions. After the shock interacts with the perturbed contact, the position errors show a linear in t behavior, i.e., a (negative) constant shock velocity error after the time $t = t_0$ of shock arrival at the contact. We observe a convergence linear in the grid spacing Δx. See Fig. 5 and the related Table 3. The columns labeled M, STD and O indicate mean, standard deviation and convergence order, in this and later tables. This implies that the true velocity error, $\text{error}_{\text{true}} = \epsilon_{\text{true}}\Delta x_{\text{coarse}}$, the difference between the exact solution and the present grid solution is double the apparent error, $\text{error}_{\text{apparent}} = \epsilon_{\text{apparent}}\Delta x$, namely the difference in shock positions between an adjacent pair of fine and coarse grid levels. In fact, for first order errors,

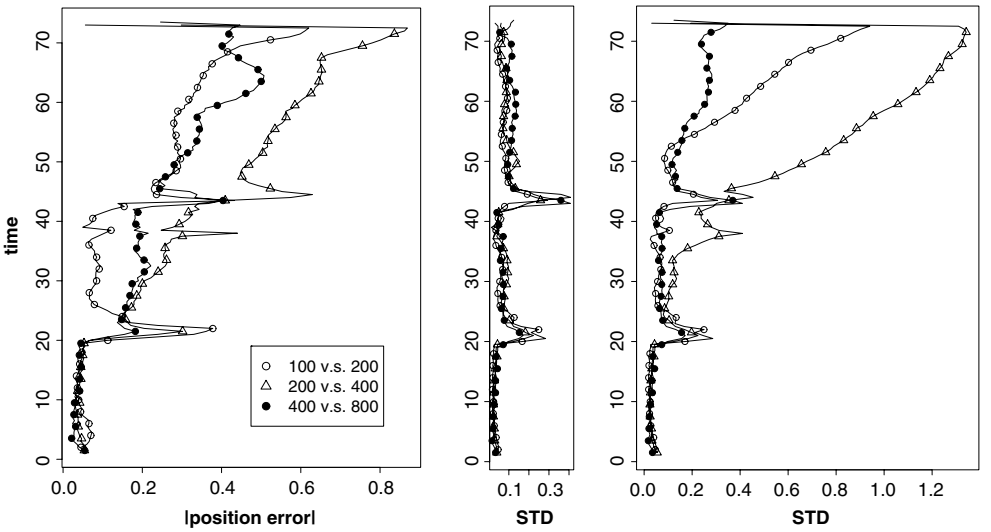

Fig. 5. Time dependent shock wave position error in units of Δx. The errors are averaged over an angular arc of size 45° near the symmetry axis and over an ensemble of $N = 5$ realizations. Both the primary (inward) and reflected (outward) shocks are shown. Observe the noise at the time of shock reflection from the origin. Non-offset case. Left: Mean errors. Center: STD of the (θ) angular variance within a single realization. Right: The STD associated with the combined ensemble and angular average of the errors (equatorial region).

Table 3
Convergence statistics for the shock position errors, averaged over time values and over an ensemble of size $N = 5$ ($^*N = 1$), in units of Δx

Grid	Inward shock			Outward shock		
	M	STD	Order	M	STD	Order
100	0.05	0.01	–	0.24	0.14	–
200	0.05	0.02	0.6	0.44	0.20	0.3
400	0.04	0.01	1.6	0.29	0.11	1.7
800*	0.04	0.01	1.0	0.24	0.13	0.6

Shock position defined relative to an angular window of size 45° at the equator, non-offset case.

$$\epsilon_{\text{true}} = \left(1 + \tfrac{1}{2} + \cdots\right)\epsilon_{\text{apparent}} = 2\epsilon_{\text{apparent}}, \tag{2}$$

after summation over all grid levels.

We fit our error data with

$$\epsilon_{\text{true}} = 2\epsilon_{\text{apparent}} = 0.016, \tag{3}$$

see Fig. 5.

To describe both angular and ensemble averages and the associated solution variability, we introduce some notation. Let

$$E_{\mathscr{I}}(e) = |\mathscr{I}|^{-1} \int_{\mathscr{I}} e(\theta, t)\, \mathrm{d}\theta \tag{4}$$

be the angular average of a function E over an angular domain $\mathscr{I}$ of length $|\mathscr{I}|$, and let

$$E_{\mathscr{E}}(e) = \int_{\mathscr{E}} e(\theta, t, \xi)\, \mathrm{d}\xi \tag{5}$$

be an average over an ensemble $\mathscr{E}$ with total mass $|\mathscr{E}| = \infty$. Then with an obvious extension of this notation, we can compose the average process to evaluate the average over both angle and ensemble, so that

$$E_{\mathscr{I}}(E_{\mathscr{E}}(e)) = E_{(\mathscr{I}\times\mathscr{E})}(e) \tag{6}$$

The related identity for variances is slightly more complicated. Let

$$\mathrm{Var}_{\mathscr{I}}(e) = |\mathscr{I}|^{-1} \int_{\mathscr{I}} (e - E_{\mathscr{I}}(e))^2 \, \mathrm{d}\theta \tag{7}$$

be the variance relative to the angular average, and similarly we define the variance $\mathrm{Var}_{\mathscr{I}\times\mathscr{E}}(e)$ relative to the combined angular and ensemble average. Then

$$\mathrm{Var}_{\mathscr{I}\times\mathscr{E}}(e) = E_{\mathscr{E}}\mathrm{Var}_{\mathscr{I}}(e) + \mathrm{Var}_{\mathscr{E}}E_{\mathscr{I}}(e). \tag{8}$$

Although the LHS of (8) is independent of the order of integration, the RHS is not, so we also have the distinct equation

$$\mathrm{Var}_{\mathscr{I}\times\mathscr{E}}(e) = E_{\mathscr{I}}\mathrm{Var}_{\mathscr{E}}(e) + \mathrm{Var}_{\mathscr{I}}E_{\mathscr{E}}(e). \tag{9}$$

Finally, we regard the standard deviation (STD $= \sqrt{\mathrm{Var}}$) as a measure of the typical fluctuations in e.

We will apply these formulas to the solution error e, in a series of grid to grid comparisons as part of a convergence study. The square root of the first term in (8) is a type of average (RMS) over the ensemble of the STD (same units as e) associated with the angular integration, and the second term displays the ensemble variability (STD) of the mean (angularly averaged) error. Similar formulas apply when the function e depends on r and when spatial and/or temporal averages are included.

We present two STDs associated with the shock position error in Fig. 5. The center frame measures the spatial fluctuations within the averaging window of 45° degrees within a single realization, i.e., the square root of the first term on the right of (8), and the right frame combines these with fluctuations of across an ensemble (of size 5) defined by varying the initial conditions. Both have size below Δx, but at late time, the larger values in the right frame indicate that the dominant variability occurs across the ensemble, and not with respect to the angle θ, except at times of times of shock passage through the interface ($t \approx 20$ and $t \approx 40$). At these times the angular dependence is dominant due to shock-interface diffraction events at a small scale (within the θ averaging window).

We find no angular dependence of the errors of the shock wave speeds on the circular angle, see Figs. 4 and 5.

4.2. Mixing zone edge errors

The mixing zone edges (and the errors in the edges) are defined as the approximate maximum and minimum radii in the mixing zone, within an angular sector. Errors in the edges of the mixing zone are shown in Fig. 6. This figure shows the error when the edge is defined relative to a 45° angular arc and averaged over an ensemble of size $N = 5$. The complex structure of the error curves in time results from timings of waves which interact with the mixing zone. The interface is shocked at $t \approx 20$ and reshocked at $t \approx 40$. The statistics of convergence averaged over time and over an ensemble of size $N = 5$ are given in Table 4. Fig. 6 and Table 4 show convergence for the mixing zone width (first order for the singly shocked portion of the mixing zone) and ambiguous or non-convergence for the centerline of the mixing zone, especially for its doubly shocked

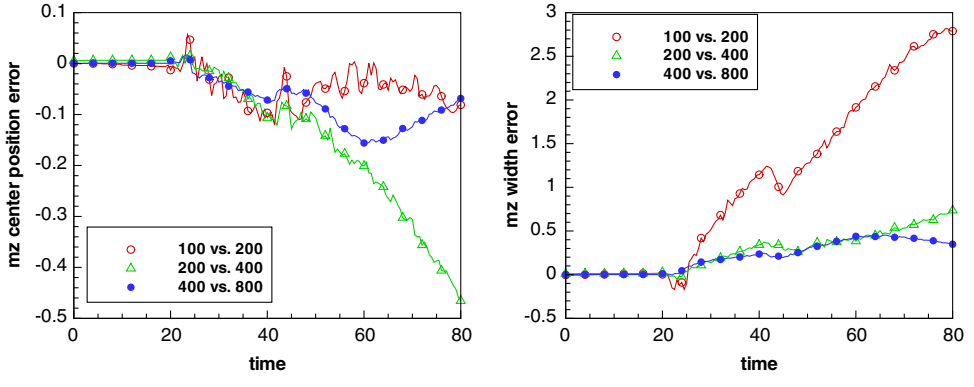

Fig. 6. Mesh convergence of the edges of the mixing zone, in units of length (cm). Non-offset case. Mixing zone defined relative to 45° window at the equator, and averaged over an ensemble of size $N = 5$. Left: Mixing zone center line. Right: Mixing zone width.

Table 4
Convergence statistics for the errors in the mixing zone edges, averaged over time values and over an ensemble of size $N = 5$ ($^*N = 1$), in units of cm

Grid	Δx	Centerline error						Width error					
		Singly shocked			Doubly shocked			Singly shocked			Doubly shocked		
		M	STD	Order	M	STD	Order	M	STD	Order	M	STD	Order
100	1/4	−0.02	0.07	–	−0.05	0.11	–	0.26	0.43	–	1.92	0.94	–
200	1/8	−0.01	0.06	0.2	−0.23	0.16	−1.0	0.08	0.17	1.5	0.45	0.72	1.0
400	1/16	−0.01	0.02	1.1	−0.10	0.19	0.2	0.07	0.09	0.8	0.35	0.35	0.9
800*	1/32	−0.01	0.01	0.9	−0.07	0.04	1.8	0.01	0.03	2.0	0.34	0.26	0.3

Edge position defined relative to an angular window $\theta \in [-45°, 0°]$. Non-offset case.

portion. Table 4 results from data collected on the angular region $\theta \in [-45°, 0°]$. Analogous data from the region $\theta \in [0°, 45°]$ shows marginal convergence (order 0.03, averaging two levels of error), most of the negative contribution coming from the coarser level error comparison. We believe this supports the idea that unusual "luck" produced atypically good coarse grid results, so that the asymptotic progression of errors as presented is perhaps misleading for the mixing zone centerline. In fact, the errors are clearly non-monotone as a function of the mesh spacing.

5. Homogeneous region error analysis

Because of the lack of interface convergence, the point values of fluid type (heavy vs. light) are not convergent in the mixing zone, and are observable only after an average, which we take to be over an angular arc of 45°. Our main conclusions regarding the spatial convergence are:

1. After average over an angular arc, the spatial variables are generally convergent, and except within shock waves and at times of wave reflection at the origin, they converge pointwise in r, t.
2. The order of convergence and its rate (that is, the coefficient of Δx for first order convergence) depend on the region (i.e., the fluid history), the degree of averaging of the observable and perhaps on the specific choice of realization from the ensemble.
3. The spatial and temporal variability in the error in general dominates the mean error. For r, t averaged errors, the ensemble does not contribute greatly to the variance of the error, but when evaluating r, t point values of the error, the ensemble variability is significant.
4. The light fluid errors ($|M| + 2$ STD) are generally larger in absolute units (g/cc) than the heavy fluid errors.

The regularity of the error in density outside of the shock wave regions can be observed in Fig. 7. We redraw this figure in Figs. 8 and 9 as a 3D plot (mean error along arc vs. radius and time). The prominent high ridges in the error are due to shock position errors, so that in these ridges, the error results from comparison of shocked with unshocked densities. Note the singularity of the light fluid error at the origin, near the time of arrival of the shock wave at the origin, as seen along the $r = 0$ axis in Fig. 9.

To compare the mean errors at different grid levels, we take a slice through the data of Figs. 8 and 9 at fixed time and present the errors as a function of radius only, see Fig. 10. The prominent shock induced errors now show up in the right frame as L_1 but not L_∞ convergent features. Outside the shock regions, the solution displays a clearly convergent, often first order behavior.

Tables 5–7 summarize statistical convergence properties of the absolute density error (units of g/cc) averaged over a 45° arc and over homogeneous regions of r, t space for a single realization and for ensemble averages. The STD is computed in terms of the single phase densities averaged over an arc of 45°. Regions directly influenced by the shock position error are excluded from this analysis. Within a single homogeneous region (e.g. singly shocked) and single fluid type (heavy or light), data for all relevant r, t are combined for the purpose of computing the mean and the STD.

The STDs are generally larger than the mean, indicating that the density error is largely random and not systematic. The error is different in the three distinct homogeneous regions, and generally smaller in the singly

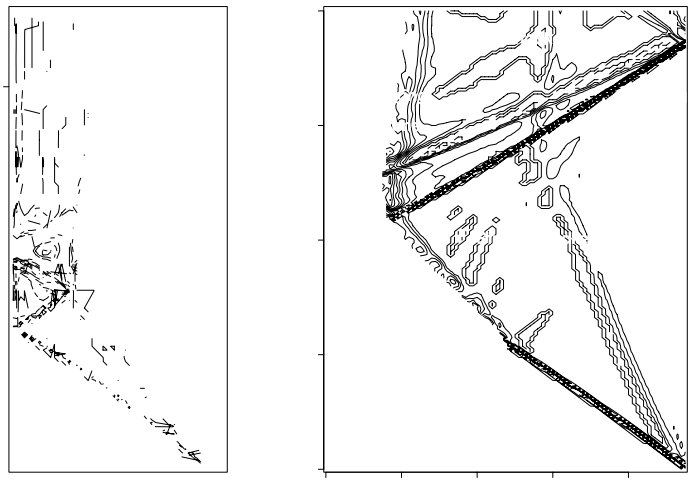

Fig. 7. Contour plots for the light (left) and heavy (right) density errors, grid level 100, non-offset case. Errors averaged over an arc of 45° at the equator for a single realization ($N = 1$).

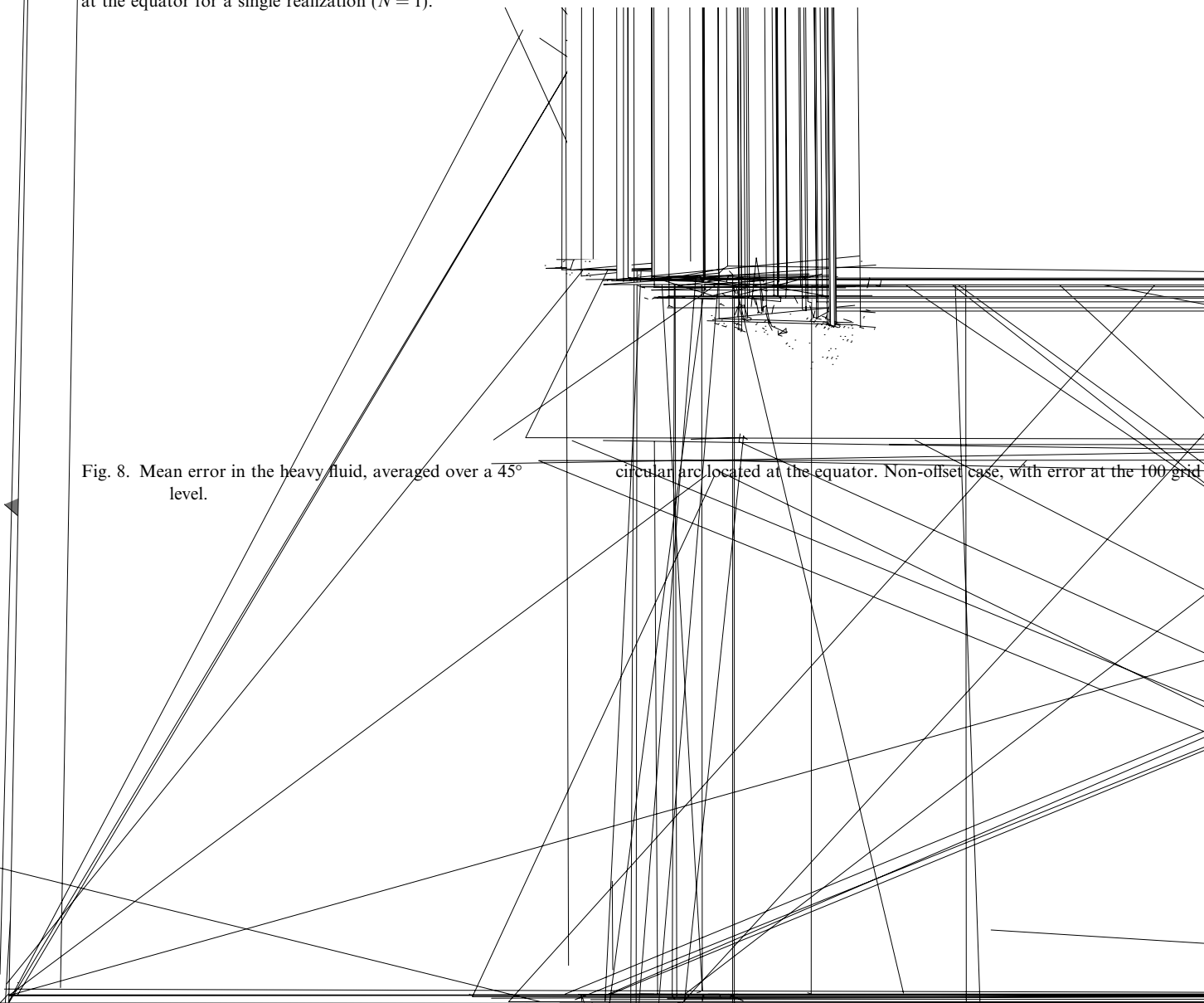

Fig. 8. Mean error in the heavy fluid, averaged over a 45° circular arc located at the equator. Non-offset case, with error at the 100 grid level.

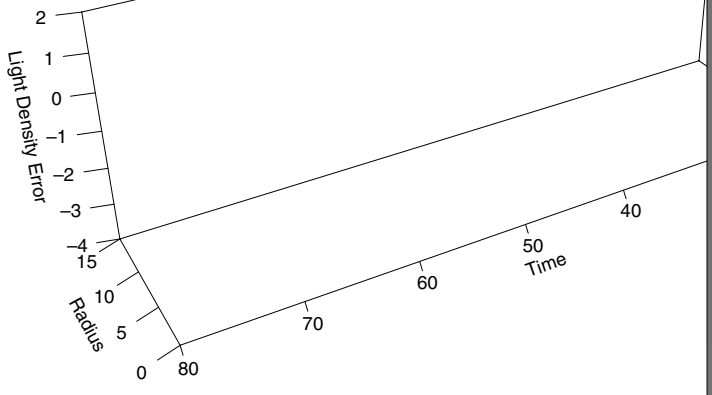

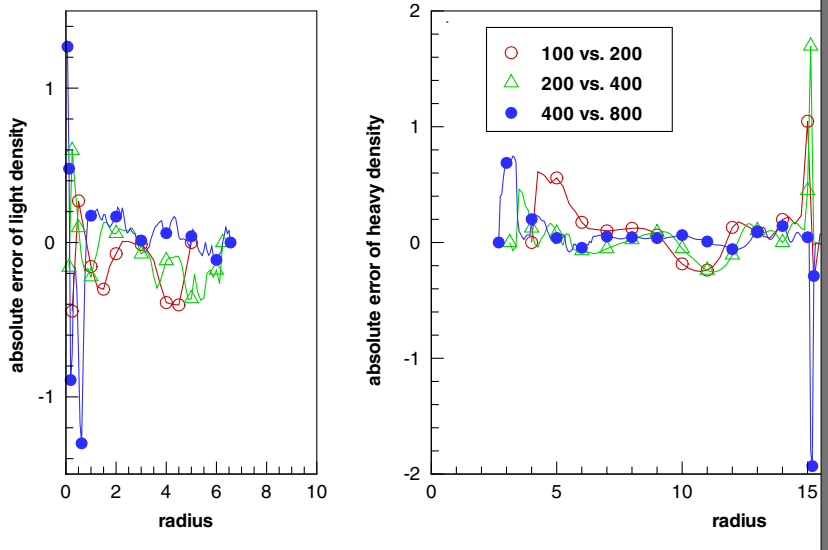

Fig. 10. Mesh convergence properties of mean density errors (g/cc), averaged over a 45° circular arc $t = 60$ and for a single realization ($N = 1$). Left: light fluid, right: heavy fluid. Note the shift of ver offset case.

6. Volume fraction error analysis

Our main results regarding the volume fraction error analysis are:

1. The single realization volume fraction are noisy and possibly non-converger
2. The ensemble averaged volume fractions are noisy but less so, and are conv
3. The singly shocked volume fraction is noticeably better that the doubly sho
4. Analytic solutions of mixed phase solutions of averaged equations suggest a v function of the radius. The current level of ensemble averaging is very far from this picture.

Table 5
Heavy fluid convergence properties averaged over the sector [0°,45°] for a single realization ($N = 1$)

Grid	Single phase						Mixing zone		
	Singly shocked			Doubly shocked					
	M	STD	Order	M	STD	Order	M	STD	Order
100	0.006	0.04	–	−0.00	0.11	–	0.29	0.29	–
200	0.001	0.03	0.5	−0.03	0.10	−0.1	0.10	0.18	0.9
400	0.000	0.02	0.6	0.03	0.04	1.1	0.10	0.21	−0.2

Mean (M), STD and convergence order (order) of the absolute error (g/cc), for various grid levels in various regions. Non-offset case.

Table 6
As with Table 5, but with averages over an ensemble of size $N = 5$

Grid	Single phase						Mixing zone		
	Singly shocked			Doubly shocked					
	M	STD	Order	M	STD	Order	M	STD	Order
100	0.002	0.05	–	0.02	0.16	–	0.36	0.27	–
200	0.001	0.03	0.7	−0.03	0.10	0.6	0.12	0.17	1.0
400	0.000	0.01	1.6	0.01	0.05	1.1	0.04	0.25	−0.2

Table 7
Light fluid convergence properties of the absolute error (in units of g/cc) for various grid levels in various regions averaged over the sector [0°,45°], over r, t in a homogeneous region, and over an ensemble of size $N = 5$

Grid	Single phase						Mixing zone		
	Singly shocked			Doubly shocked					
	M	STD	Order	M	STD	Order	M	STD	Order
100	−0.02	0.05	–	−0.02	0.38	–	−0.21	0.20	–
200	−0.03	0.04	0.3	−0.04	0.28	0.4	−0.06	0.17	0.6
400	−0.01	0.02	1.2	−0.01	0.29	0.0	−0.02	0.10	0.8

Non-offset case.

Table 8
Percent contributions of three terms to the total variance for the heavy fluid convergence, non-offset case, equatorial region, ensemble size $N = 5$

Grid	100	200	400	Grid	100	200	400
Singly shocked							
Var_r	83	88	91	$\mathrm{Var}_\mathscr{E}$	12	13	04
Var_t	16	11	09	Var_r	75	78	87
$\mathrm{Var}_\mathscr{E}$	01	01	00	Var_t	14	09	09
Doubly shocked							
Var_r	61	56	84	$\mathrm{Var}_\mathscr{E}$	36	75	39
Var_t	28	28	14	Var_r	41	21	50
$\mathrm{Var}_\mathscr{E}$	11	16	02	Var_t	23	04	11
Mixed region							
Var_r	34	80	94	$\mathrm{Var}_\mathscr{E}$	46	68	76
Var_t	48	17	05	Var_r	08	26	22
$\mathrm{Var}_\mathscr{E}$	18	03	02	Var_t	46	06	02

The value for each term depends on its order of evaluation; here we evaluate the variances starting from the top in two possible orders.

In Figs. 11–13, left, we show the volume fraction as a function of scaled radius at three time values, as mesh spacing is varied. The scaling of the radius ensures that the horizontal axis varies from 0 to 1 as one passes through the mixing zone. The purpose of this presentation of the data is to remove from the present plots the variability associated with the edges of the mixing zone, already analyzed in Section 4.2. In the right

Table 9
Percent contributions of three terms to the total variance for the light fluid convergence, non-offset case, equatorial region, ensemble size $N = 5$

Grid	100	200	400	Grid	100	200	400
Singly shocked							
Var_r	31	45	70	$\mathrm{Var}_\mathscr{E}$	54	70	71
Var_t	41	20	22	Var_r	14	21	19
$\mathrm{Var}_\mathscr{E}$	28	35	08	Var_t	32	09	10
Doubly shocked							
Var_r	68	69	85	$\mathrm{Var}_\mathscr{E}$	31	48	60
Var_t	24	24	07	Var_r	45	36	35
$\mathrm{Var}_\mathscr{E}$	08	07	08	Var_t	24	16	05
Mixed region							
Var_r	44	54	81	$\mathrm{Var}_\mathscr{E}$	46	72	59
Var_t	54	28	18	Var_r	19	11	27
$\mathrm{Var}_\mathscr{E}$	11	18	01	Var_t	35	17	14

The value for each term depends on its order of evaluation; here we evaluate the variances starting from the top in two possible orders.

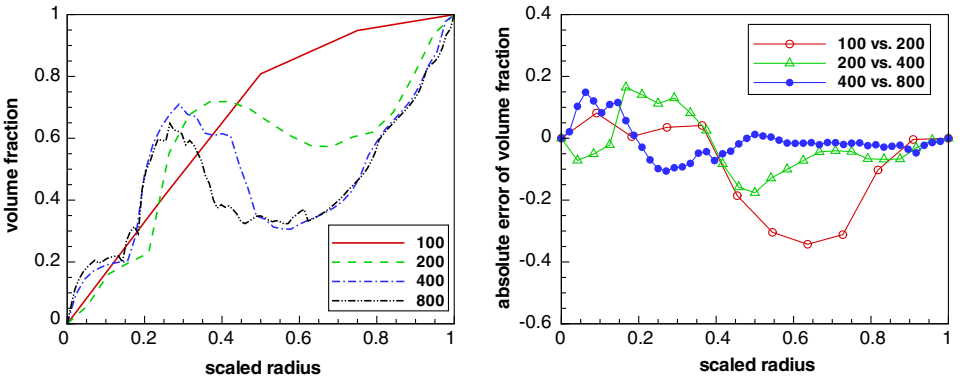

Fig. 11. Volume fraction (left) and errors (right) plotted vs. scaled distance through the mixing zone, for the heavy fluid for four grid levels (three levels for the error), ensemble averaged ($N = 5$), non-offset case, equatorial region, $t = 40$.

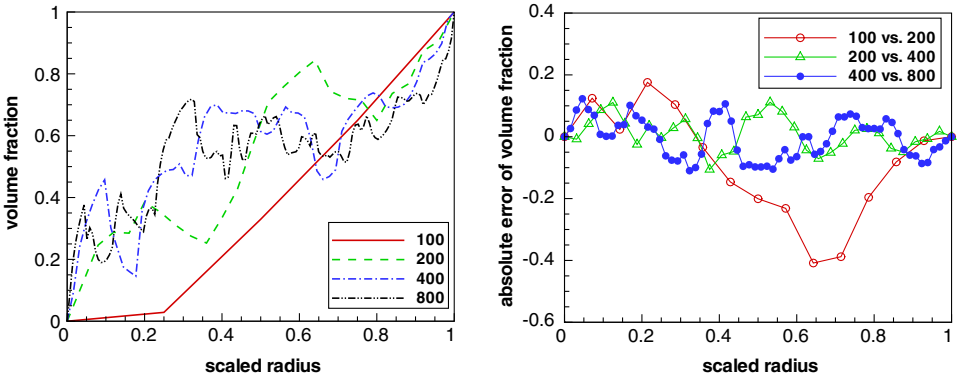

Fig. 12. Volume fraction (left) and errors (right) plotted vs. scaled distance through the mixing zone, for the heavy fluid for four grid levels (three levels for the error), ensemble averaged ($N = 5$), non-offset case, equatorial region, $t = 60$.

frames, we show the time plots of the resulting solution errors for the volume fraction, all averaged over an ensemble of $N = 5$ realizations, and also plotted vs. a scaled radius. The convergence statistics computed by comparison of the βs at the same value of scaled radius (not of radius itself), and summarized in Table 10, shows near first order convergence for the volume fraction in the singly shocked region and marginal or half

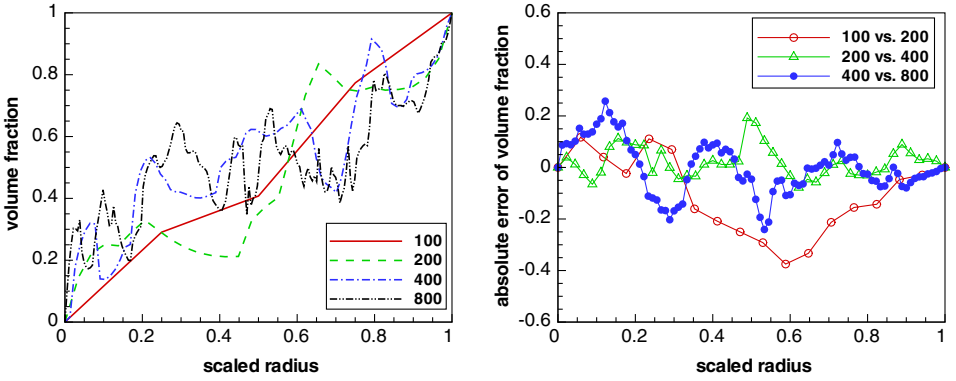

Fig. 13. Volume fraction (left) and errors (right) plotted vs. scaled distance through the mixing zone, for the heavy fluid for four grid levels (three levels for the error), ensemble averaged ($N = 5$), non-offset case, equatorial region, $t = 80$.

Table 10
Volume fraction (of heavy fluid) convergence properties. Absolute error for an ensemble of size $N = 5$

Grid	M	STD	Order	$\mathrm{Var}_{\mathscr{E}}$	Var_r	Var_t
Singly shocked						
100	0.03	0.10	–	48	48	8
200	0.03	0.06	0.6	66	33	1
400	0.02	0.04	0.6	45	49	6
Doubly shocked						
100	−0.05	0.10	–	49	49	2
200	0.00	0.06	1.1	83	16	1
400	0.02	0.07	−0.6	70	29	1

The last three columns are percent contributions to the total variance computed in the order $\mathscr{E}$, r, t, i.e. left to right. Non-offset case, data from equatorial region.

order convergence in the doubly shocked region. The right columns of this table illustrate the importance of the ensemble average, as the quantity $\mathrm{Var}_{\mathscr{E}}$ is a significant or dominant part of the total variance of the r, t point values of the volume fraction. For example, averaging over grid levels, the ensemble average accounts for about 70% of the volume fraction variability.

References

[1] I. Babuska, W. Rheinboldt, A posteriori error estimates for the finite element method, Int. J. Numer. Meth. Eng. 12 (1978) 1597–1615.
[2] G. Batchelor, The Theory of Homogeneous Turbulence, The University Press, Cambridge, 1955.
[3] L. Bonet-Cunha, D.S. Oliver, R.A. Redner, A.C. Reynolds, A hybrid markov chain Monte Carlo method for generating permeability fields conditioned to multiwell pressure data and prior information, SPE J. 3 (1998) 261–271.
[4] B. Cockburn, H. Gau, A posteriori error estimates of general numerical methods for scalar conservation laws, Math. Appl. Comp. 14 (1995) 37–47.
[5] P.S. Craig, M. Goldstein, J.C. Rougier, A.H. Seheult, Bayesian forecasting for complex systems using computer simulators, J. Am. Stat. Assoc. 96 (2001) 717–729.
[6] B. Debusschere, H. Najm, P. Pebay, O.K.R. Ghanem, O.L. Maitre, Numerical challenges in the use of polynomial chaos representations for stochastic processes, SIAM J. Sci. Comput. 26 (2) (2004) 698–719.
[7] J. Glimm, J.W. Grove, Y. Kang, T. Lee, X. Li, D.H. Sharp, Y. Yu, K. Ye, M. Zhao, Statistical Riemann problems and a composition law for errors in numerical solutions of shock physics problems, SISC 26 (2004) 666–697, University at Stony Brook Preprint Number SB-AMS-03-11, Los Alamos National Laboratory number LA-UR-03-2921.
[8] J. Glimm, J.W. Grove, Y. Kang, T. Lee, X. Li, D.H. Sharp, Y. Yu, K. Ye, M. Zhao, Errors in numerical solutions of spherically symmetric shock physics problems, Contemp. Math. 371 (2005) 163–179, University at Stony Brook Preprint Number SB-AMS-04-03, Los Alamos National Laboratory number LA-UR-04-0713.
[9] J. Glimm, D.H. Sharp, Stochastic methods for the prediction of complex multiscale phenomena, Quart. J. Appl. Math. 56 (1998) 741–765.

[10] J. Glimm, D.H. Sharp, Prediction and the quantification of uncertainty, Physica D 133 (1999) 152–170.
[11] B.K. Hegstad, H. Omre, Uncertainty assessment in history matching and forecasting, in: E.Y. Baafi, N.A. Schofield (Eds.), Geostatistics Wollongong '96, Kluwer Academic Publishers, 1997, pp. 585–596.
[12] M.C. Kennedy, A. O'Hagan, Bayesian calibration of computer models, J. Roy. Stat. Soc. Ser. B 63 (2001) 425–450.
[13] L. Lake, Enhanced Oil Recovery, Prentice-Hall, Englewood Cliffs, 1989.
[14] D. Lucor, C.-H. Su, G.E. Karniadakis, Generalized polynomial chaos and random oscillators, Int. J. Numer. Meth. Eng. 60 (3) (2004) 571–596.
[15] D. Martinson, K. Bryan, M. Ghil, M. Hall, T. Karl, E. Sarachik, S. Sorooshian, L. Talley (Eds.), Natural Climate Variability on Decade-to-Century Time Scales, National Academy Press, 1995.
[16] W.D. McComb, The Physics of Fluid Turbulence, Oxford University Press, Oxford, 1990.
[17] J.C. Niemeyer, W. Hillebrandt, Turbulent nuclear flames in Type Ia supernovae, ApJ 452 (1995) 769–778.
[18] J.T. Oden, M. Ainsworth, A Posteriori Error Estimation in Finite Element Analysis, John Wiley & Sons, New York, 2000.
[19] M. Reagan, H. Najm, B. Debusschere, O.L. Maitre, O. Knio, R. Ghanem, Spectral stochastic uncertainty quantification in chemical systems, Combust. Theor. Model. 8 (2004) 607–632.
[20] D.H. Sharp, An overview of Rayleigh–Taylor instability, Physica D 12 (1984) 3–18.
[21] K. Veroy, A.T. Patera, Certified real-time solution of the parametrized steady incompressible Navier–Stokes equations: Rigorous reduced-basis a posteriori error bounds, Int. J. Numer. Meth. Fluids 47 (2005) 773–788.
[22] G.B. Whitham, Linear and Nonlinear Waves, John Wiley & Sons, New York, 1974.
[23] D. Xiu, D. Lucor, C.-H. Su, G.E. Karniadakis, Stochastic modeling of flow-structure interactions using generalized polynomial chaos, J. Fluid. Eng. 124 (2002) 51–59.